

Identification of Central-Pacific and Eastern-Pacific types of ENSO in CMIP3 models

Jin-Yi Yu¹ and Seon Tae Kim¹

Received 23 May 2010; revised 18 June 2010; accepted 7 July 2010; published 13 August 2010.

[1] Much understanding of the El Niño–Southern Oscillation (ENSO) has been obtained from the analyses of the climate simulations produced for World Climate Research Programme’s Coupled Model Intercomparison Project phase 3 (CMIP3). However, most of these analyses do not consider the existence of the Eastern-Pacific (EP) and Central-Pacific (CP) types of ENSO events, which have been increasingly recognized as two distinct types of interannual sea surface temperature (SST) variation in the tropical Pacific. This study uses a regression–Empirical Orthogonal Function method to identify how well these two ENSO types are captured in the pre-industrial simulations of nineteen CMIP3 models. It is concluded that most CMIP3 models (13 out of 19) can produce realistically strong CP ENSOs, but only a few of them (9 out of 19) can produce realistically strong EP ENSOs. Six models that realistically simulate both the EP and CP ENSOs and their intensity ratio are identified. By separating the SST variability into these two types, it is further revealed that the leading periodicity of the simulated EP ENSO is linearly related to the latitudinal width of SST variability and varies from 1 to 5 years. As for the simulated CP ENSO, its leading periodicity is either 2 or 4 years depending on whether its SST variability is located to the east of the dateline or in the western-Pacific warm pool, respectively. The identification produced in this study offers useful information to further understand the two types of ENSO using the CMIP3 models. **Citation:** Yu, J.-Y., and S. T. Kim (2010), Identification of Central-Pacific and Eastern-Pacific types of ENSO in CMIP3 models, *Geophys. Res. Lett.*, 37, L15705, doi:10.1029/2010GL044082.

1. Introduction

[2] Significant advances in climate research have been obtained from analyses of the simulations produced for the World Climate Research Programme’s (WCRP’s) Coupled Model Intercomparison Project phase 3 (CMIP3), comprised of extended integrations with 24 coupled atmosphere–ocean general circulation models (CGCMs). Many studies have analyzed the El Niño–Southern Oscillation (ENSO) simulations produced by these models and have reported models’ successes and deficiencies in capturing the observed features of ENSO [e.g., *Guilyardi et al.*, 2009]. However, most of the analyses do not consider the existence of two different types of ENSO events, which has been increasingly suggested by recent studies [*Larkin and Harrison*, 2005; *Yu and Kao*, 2007; *Ashok et al.*, 2007; *Kao and Yu*, 2009; *Kug et al.*,

2009]. These two types include a conventional ENSO type [*Rasmusson and Carpenter*, 1982] that has its primary sea surface temperature (SST) anomalies centered in the eastern Pacific, and a non-conventional ENSO type that has SST anomalies confined more to the central Pacific. *Kao and Yu* [2009] refer to these two types as the Eastern-Pacific (EP) and Central-Pacific (CP) types, respectively. It should be mentioned that different flavors of ENSO have been noticed before these recent studies. *Trenberth and Stepaniak* [2001], for example, were among the first to recognize that the different characters and evolutions of ENSO events could not be fully accounted for without considering the SST contrast between the eastern and central equatorial Pacific. However, there is still no documentation of how well these two types of ENSO events are captured in the CMIP3 models. Such documentation could be useful for selecting CMIP3 models to study these two types of ENSO events. The purpose of this study is to provide such documentation and to demonstrate new information on ENSO simulations that can be obtained by taking this two-ENSO view.

2. Data

[3] Pre-industrial integrations produced by the CMIP3 models are analyzed in this study, in which greenhouse gases are held fixed at pre-industrial levels. Nineteen CMIP3 CGCMs are analyzed in this study, excluding five that show little interannual SST variability in the tropical Pacific. For comparison purposes, only 100 years of the integrations are analyzed. For the observational SST, we use Extended Reconstruction of Historical Sea Surface Temperature version 3 (ERSST V3) data [*Smith and Reynolds*, 2003] and Met Office Hadley Centre Sea Ice and Sea Surface Temperature data (HadISST) [*Rayner et al.*, 2003] over the period of 1950–2009. Monthly SST anomalies from the observations and the pre-industrial simulations are computed by removing the monthly mean climatology and the trend.

3. Results

[4] Following *Kao and Yu* [2009], we apply a combined regression–Empirical Orthogonal Function (EOF) analysis (similar to the conditional EOF of *An* [2003]) to the monthly SST anomalies to identify the EP and CP types of ENSO events. We first remove the tropical Pacific SST anomalies that are regressed with the Niño-4 SST index and then apply the EOF to the residual SST anomalies to obtain the SST anomaly pattern for the EP ENSO. Similarly, the SST anomaly pattern of the CP ENSO is obtained by applying the EOF to the residual SST anomalies after the anomalies regressed with the Niño1+2 SST index are removed. Different from *Kao and Yu* [2009], we remove not only the

¹Department of Earth System Science, University of California, Irvine, California, USA.

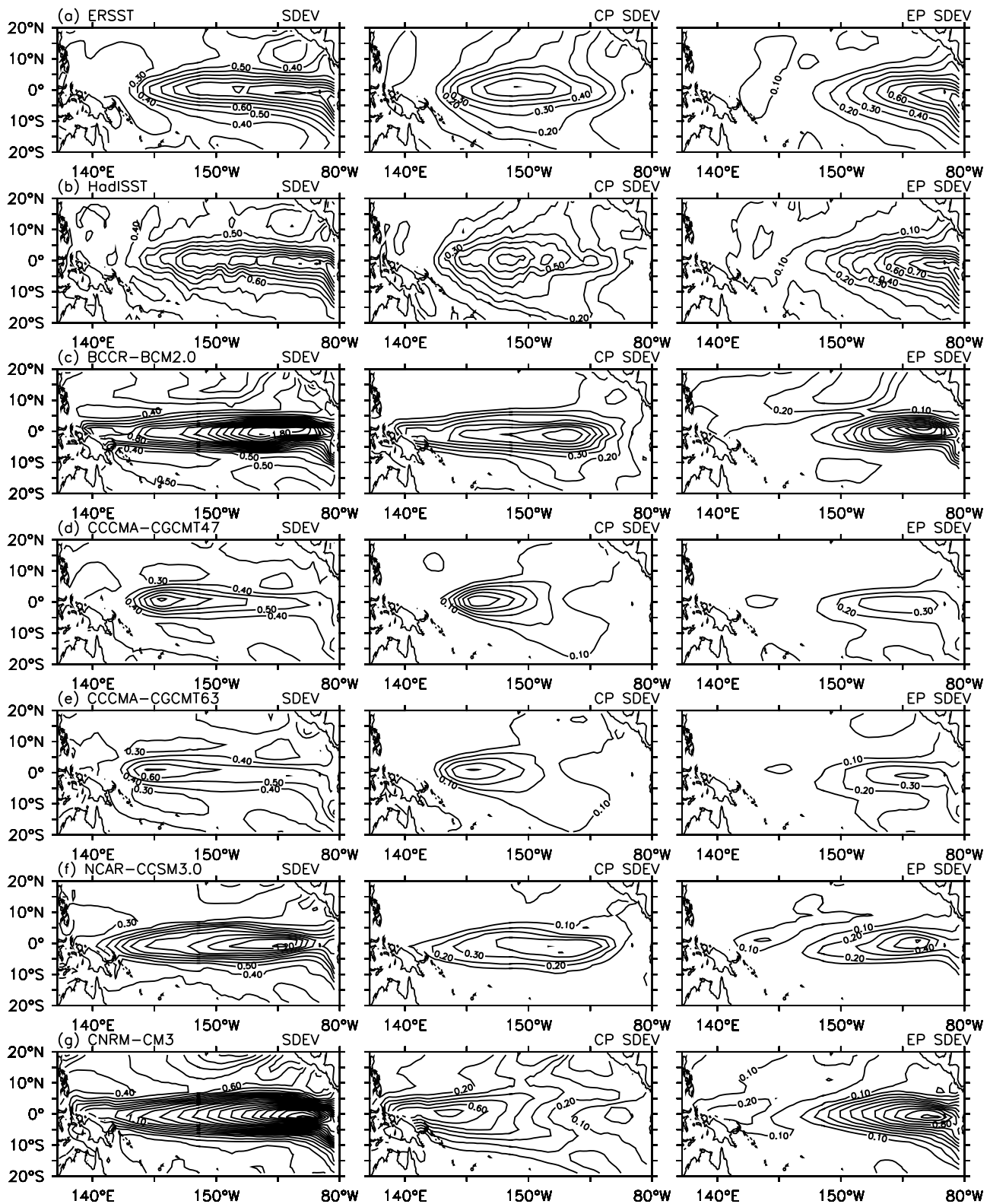


Figure 1. (left) Spatial patterns of total standard deviations of tropical SST anomalies and standard deviations of the first EOF mode for the (middle) CP ENSO and (right) EP ENSO calculated from the observation and nineteen CMIP3 models.

simultaneous regression but also the regression at lag -3, -2, -1, +1, +2, and +3 months to consider the propagation of SST anomalies between the central and eastern Pacific, although the results are not very different with or without

these additional removals. Figure 1 shows the results obtained from this regression-EOF analysis. Figure 1 (left panels) shows the total standard deviation (STD) of the interannual SST anomalies, and Figures 1 (middle panels)

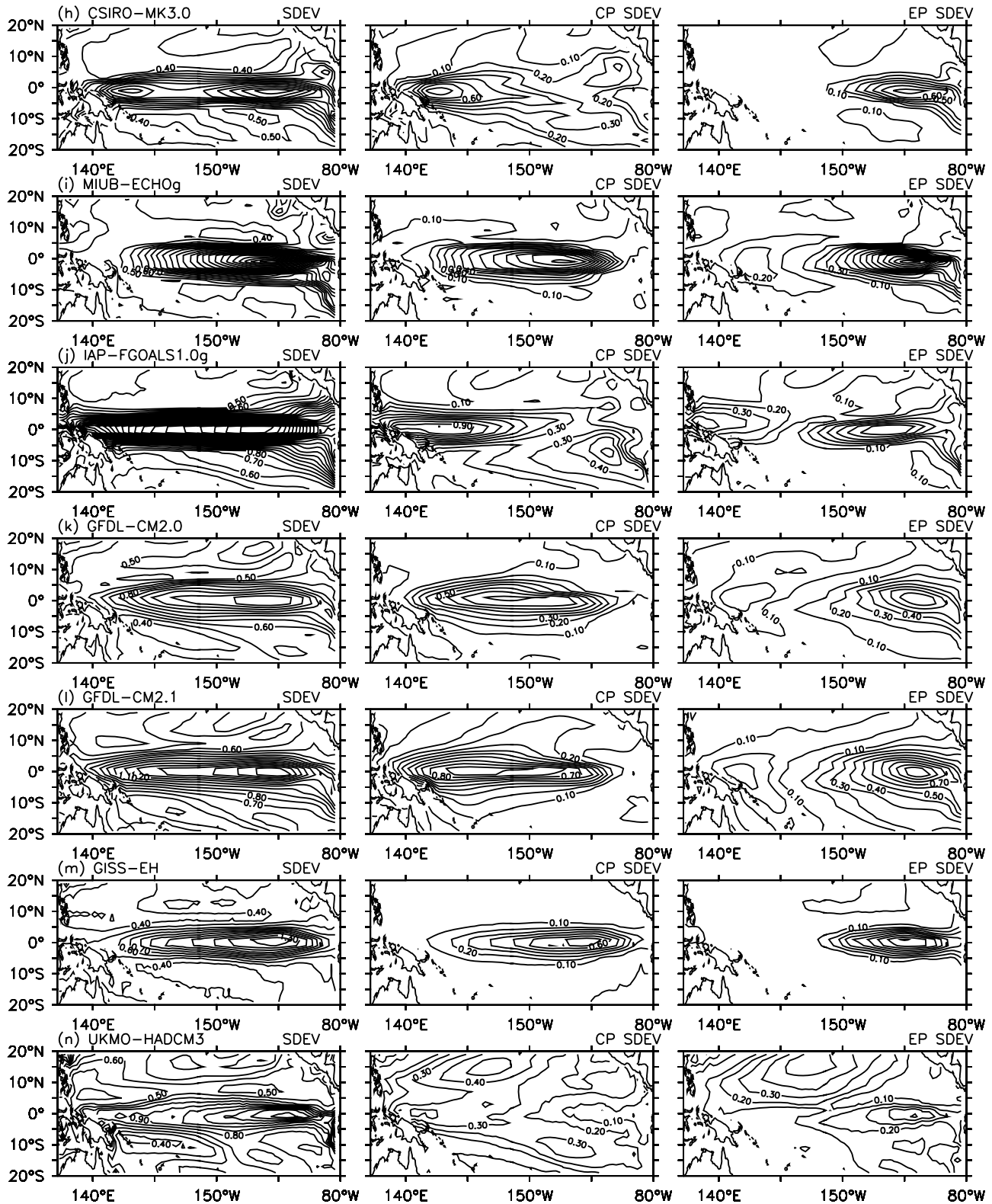


Figure 1. (continued)

and 1 (right panels) show, respectively, the leading EOF modes of the CP and EP ENSOs. The loading coefficients shown in the EOFs are scaled by their Eigenvalues to reflect the SST STD at each grid point. Most previous studies of

CMIP3 model simulations used the total SST variability to examine the ENSO simulations. But a different picture emerges when we separate the variability into the EP and CP types. For example, CCCMA-CGCM2.4.7 (Figure 1d) may

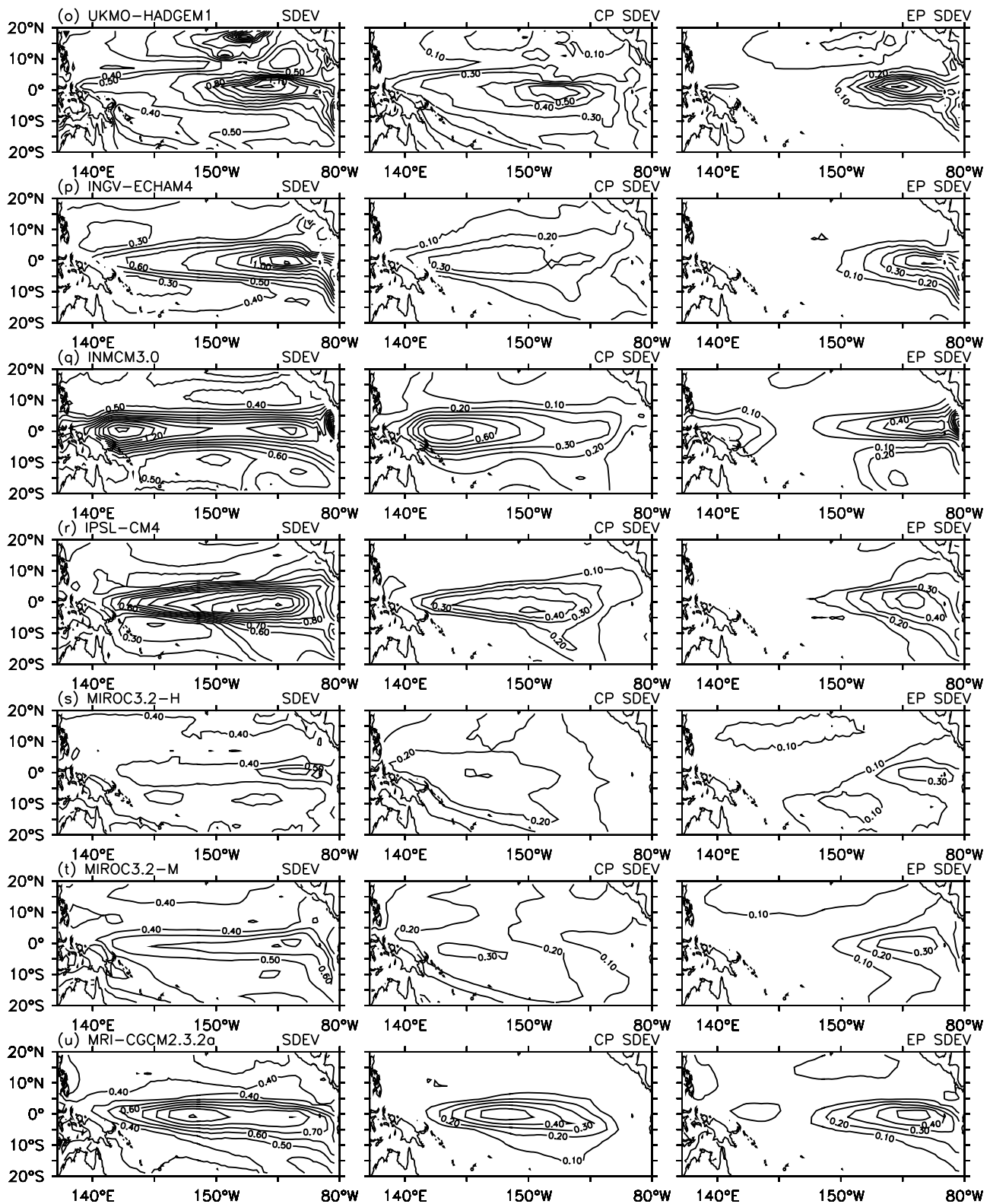


Figure 1. (continued)

appear to have its simulated ENSO displaced too far westward if it is judged based on the total SST variability. But after separating the variability into the EP and CP types, we find that both the EP and CP ENSO patterns are reasonably close to the observations. Nevertheless, the simulated

intensity of the EP ENSO is too weak, which leads to the too-far-westward appearance of the total SST variability. We have also calculated the correlation coefficients between the principal components of the leading EP and CP EOFs and find them to be small for most models (the mean cor-

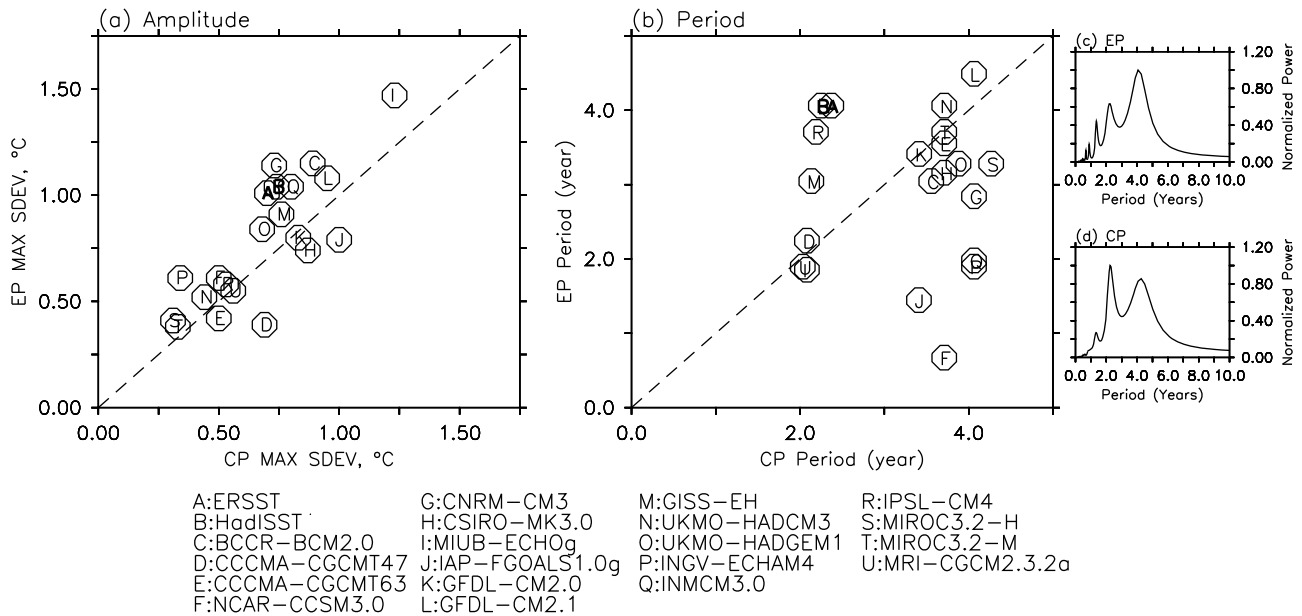


Figure 2. Scatter plot of (a) maximum standard deviation (STD) and (b) the leading periods for EP versus CP ENSO from models and observations, and the normalized power spectrum for the observed (c) EP and (d) CP ENSOs from the ERSST. The maximum STD is identified from a latitudinal band between 10°N and 10°S in Figures 1 (middle) and 1 (right).

relation is 0.26), which indicates that the EP and CP ENSOs are reasonably separated by the regression-EOF method.

[5] In the observations (Figures 1a and 1b), the EP ENSO is characterized by SST variability extending from the South American Coast into the central Pacific along the equator. The observed CP ENSO has most of its SST variability located in the central tropical Pacific (between 160°E and 120°W) and extends towards the subtropics of both hemispheres. Most of the models produce an EP ENSO similar to the observations, except their latitudinal widths can differ from the observations. The pattern correlation between the simulated EP ENSO and the observed one varies from 0.21 (UKMO-HADCM3) to 0.93 (INGV-ECHAM4), with an average of 0.75. For the CP ENSO, some models can capture the poleward extension of the SST variability pattern, but some have the variability more confined near the equator. Furthermore, some simulated CP ENSOs are located in the western Pacific warm pool and others towards the international dateline. The average pattern correlation coefficient is 0.62.

[6] We then calculate the maximum STD values from Figures 1 (middle) and 1 (right) to quantify the intensities of the observed and simulated EP and CP ENSOs. Figure 2a displays the EP versus CP ENSO intensity through a scatter diagram. The observed intensities (averages of Points A and B in Figure 2a) are about 0.7°C for the CP ENSO and 1.0°C for the EP ENSO. The ratio of the EP-to-CP ENSO intensities is about 1.4, which means the EP ENSO dominates the CP ENSO by about 40% in intensity. We use the lower limit of the 95% significance interval of the observed ENSO intensities (based on an F-test) as the criteria to determine which CMIP3 models produce realistically strong EP and CP ENSOs. The lower 95% limit values are 0.78°C for the EP type and 0.51°C for the CP type. Based on these criteria, there are nine models (CNRM-CM3, INMCM3.0, BCCR-BCM2.0, UKMO-HADGEM1, GISS-EH, MIUB-ECHOg,

GFDL-CM2.1, GFDL-CM2.0, and IAP-FGOALS1.0g) that can simulate both types of ENSO events with strong intensities. Another four models can produce only strong CP ENSOs: CCCMA-CGCM-T47, CSIRO-MK3.0, IPSL-CM4, and MRI-CGCM2.3.2a. The remaining six models (CCCMA-CGCM-T63, NCAR-CCSM3.0, UKMO-HADCM3, INGV-ECHAM4, MIROC3.2-H, and MIROC3.2-M) produce both types of ENSO events with weak intensities under our separation method.

[7] We can also examine the ratio of the EP-to-CP ENSO intensities in Figure 2a. Among the nine models that produce strong enough EP and CP ENSOs, we find that six models (BCCR-BCM2.0, CNRM-CM3, GFDL-CM2.1, GISS-EH, UKMO-HADGEM1, and INMCM3.0) produce the most realistic intensity ratios. They are indicated in Figure 2a as Points C, G, L, M, O, and Q, which are most close to the observation points (A and B). Based on the intensity ratio alone, we find seven models whose EP type dominates the CP type (i.e., the intensity ratio > 1) in their ENSO simulations. The other twelve models have the CP type dominates the EP type (i.e., the intensity ratio < 1). Therefore, most of the CMIP3 models produce stronger CP ENSO relative to EP ENSO.

[8] To demonstrate that separating the EP and CP types of ENSO in the CMIP3 simulations can reveal new information, we look further into the leading periodicities of these two ENSO types. Figure 2b displays the scatter diagram of the leading periodicity of the EP ENSO versus that of the CP ENSO for the nineteen CMIP3 models and the two observed SST data sets. The leading periodicity is determined by performing a power spectrum analysis of the principal component of the leading SST EOF modes of the two ENSO types. Shown in Figures 2c and 2d are the power spectra calculated from the ERSST data set for the EP and CP ENSOs. For the observed EP ENSO (Figure 2c), the power spectrum is dominated by a peak near 4 years. For the

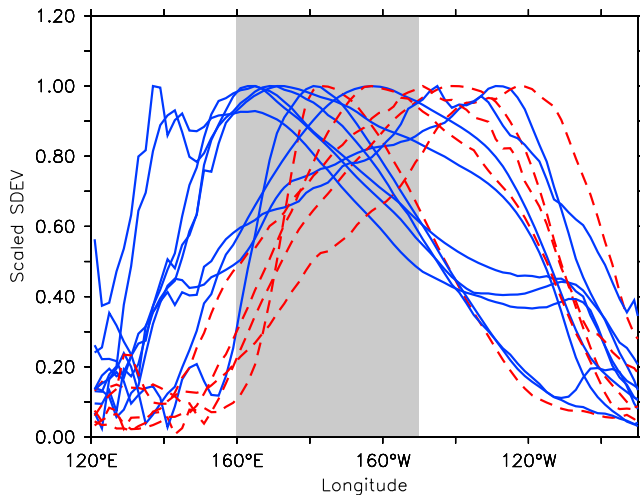


Figure 3. Zonal distributions of equatorial (5°S–5°N) SST variability of the leading EOF mode of the CP ENSO calculated from Figure 1 (middle). Values shown are scaled by their maximum value. Blue (red) curves represent models whose CP ENSO has a 4-year (2-year) leading period. Shading region indicates the NINO4 region.

observed CP ENSO (Figure 2d), the power spectrum has two comparable peaks: one near 2 years and the other near 4 years. The 2-year peak has a larger power than the 4-year peak. Therefore, in Figure 2b the ERSST (Point A) is shown to have a leading period of 2 years for the CP ENSO and a leading period of 4 years for the EP ENSO. Similar leading periodicities are found from the HadISST data (Point B). Interestingly, it is noticed from the scatter diagram that the leading periods of the simulated CP ENSOs are grouped into two periods, namely, 2 and 4 years, which are the two major periods found in the observed CP ENSO. This result indicates that one group of CMIP3 models captures the 2-year component of the observed CP ENSO and the other group produces the 4-year component.

[9] We inspect the SST variability patterns in Figure 1 for these two groups of models and notice an interesting difference: the models that produce the 4-year CP ENSO tend to have their SST variability located towards the western-Pacific warm pool, while the models that produce the 2-year CP ENSO tend to have their SST variability located to the east of the international dateline. This difference is better revealed in Figure 3, which shows the zonal distribution of the equatorial (5°S–5°N) SST variability calculated from the leading EOF mode of the CP ENSO (Figure 1, middle) for the thirteen CMIP3 models that produce a realistically strong CP ENSO. The values shown are normalized by the respective maximum value of each distribution. The blue-solid lines in Figure 3 represent the models whose CP ENSO has a 4-year leading period, while the red-dashed lines indicate those whose CP ENSO has a 2-year leading period. Figure 3 shows that most of the red-dashed lines have their peak SST variability centered between 160°W and 120°W, while most of the blue-solid lines have their peak variability centered between 120°E and 160°E. These results suggest that there are two variants of the CP ENSO: a warmpool-CP and a dateline-CP, which are separated by different leading periodicities and different SST variability

centers. Further studies are needed to better understand how these two variants of CP ENSO are produced and why some CMIP3 models produce one but not the other.

[10] From Figure 2b, we also notice that the leading period of the simulated EP ENSO can vary from close to one year to more than 4 years, while the observations show a 4-year leading periodicity. We inspect the EP ENSO patterns in Figures 1 and notice the leading periodicity seems to be related to the latitudinal width of the SST variability of the EP ENSO. This linkage is verified in Figure 4, where the leading periodicity of the EP ENSOs simulated by the nine CMIP3 models that produce strong EP ENSOs versus the latitudinal width (L_y) of their SST variability is shown. Here L_y is defined as the e-folding width of the maximum value of the EP SST variability. A linear relationship appears among these scatter points, which shows the larger the latitudinal width, the longer the EP ENSO period. This is consistent with the suggestion of *Kao and Yu [2009]* that the EP ENSO is produced by subsurface variation processes similar to those described by recharge-discharge theory [*Jin, 1997*]. According to this theory, the EP ENSO acts as a mechanism to remove excess ocean heat contents from the equatorial to the off-equatorial Pacific. Therefore, when a wider latitudinal range is involved in the SST variability, it takes longer to complete the recharge-discharge process resulting in a longer periodicity for the ENSO. This result is also consistent with previous studies that showed ENSO period is related to the latitudinal width of the wind stress anomalies [e.g., *Kirtman, 1997; Capotondi et al., 2006; Neale et al., 2008*].

4. Summary and Discussion

[11] In this study, we examined the pre-industrial simulations produced by nineteen CMIP3 models to document how well these models capture the EP and CP types of ENSO events. Based on the intensity information, the CMIP3 models can be separated into groups that produce both CP and EP ENSOs that are realistically strong (nine

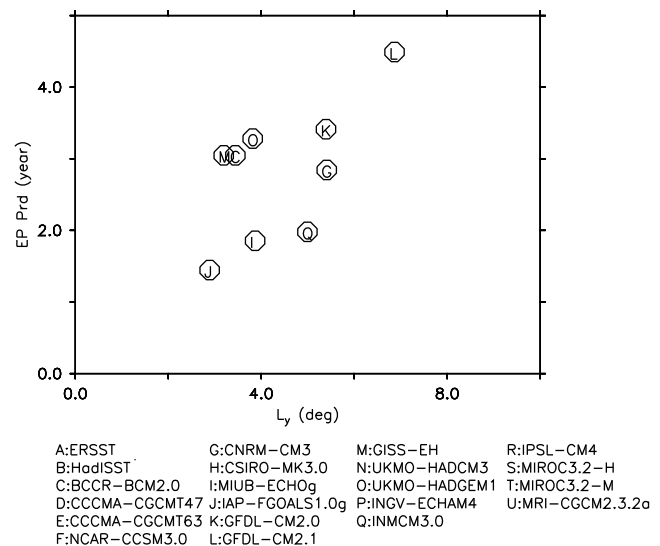


Figure 4. Leading periods of EP ENSO versus the meridional widths of their SST variability from the nine CMIP3 models that produce strong enough EP ENSO.

models), only CP ENSOs that are realistically strong (four models), CP ENSOs that are too weak (six models), EP ENSO that are too weak (ten models), and realistic EP-to-CP ENSO intensity ratios (six models). This grouping information helps to determine which CMIP3 models should be used to study the EP ENSO, CP ENSO, and their interactions. By separating ENSO SST variability into the EP and CP types, we find two interesting features in the simulated ENSO periodicity. The period of the simulated EP ENSO varies between 1 and 5 years and is linearly related to the latitudinal width of its SST variability pattern. But no such connection is found for the simulated CP ENSO, whose periodicity can only be 2 or 4 years. Although we do not know the reason for this period selection, we found that the selection is related to location of the center of the CP ENSO variability. The longer 4-year CP ENSO is located over the warm pool and the shorter 2-year CP ENSO is located to the east of the dateline. This interesting result supports the suggestion that the CP ENSO is not generated by the thermocline variation mechanism. Otherwise, the warmpool-CP ENSO should have a shorter period than the dateline-CP ENSO because the former is located closer to the western Pacific and should be influenced by the thermocline wave reflection and propagation sooner than the latter [An and Wang, 2000]. In conclusion, the identification produced by this study offers information that can be useful for using CMIP3 models to study the dynamics of EP and CP ENSOs. It should be noted that the results reported in this study are obtained from 100 years of pre-industrial integrations, which may not necessarily be the same in different centuries of model simulations due to the decadal and century timescale variability of ENSO events [e.g., Knutson and Manabe, 1998; Timmermann, 1999; Meehl et al., 2006].

[12] **Acknowledgments.** We thank two anonymous reviewers for their helpful comments. This research was supported by NSF (ATM-0925396). We acknowledge the modeling groups, the Program for Climate Model Diagnosis and Intercomparison (PCMDI) and the WCRP's Working Group on Coupled Modelling (WGCM) for their roles in making available the WCRP CMIP3 multi-model dataset.

References

- An, S.-I. (2003), Conditional maximum covariance analysis and its application to the tropical Indian Ocean SST and surface wind stress anomalies, *J. Clim.*, *16*, 2932–2938, doi:10.1175/1520-0442(2003)016<2932:CMCAAI>2.0.CO;2.
- An, S.-I., and B. Wang (2000), Interdecadal change of the structure of the ENSO mode and its impact on the ENSO frequency, *J. Clim.*, *13*, 2044–2055, doi:10.1175/1520-0442(2000)013<2044:ICOTSO>2.0.CO;2.
- Ashok, K., S. Behera, A. S. Rao, H. Weng, and T. Yamagata (2007), El Niño Modoki and its teleconnection, *J. Geophys. Res.*, *112*, C11007, doi:10.1029/2006JC003798.
- Capotondi, A., A. Wittenberg, and S. Masina (2006), Spatial and temporal structure of tropical Pacific interannual variability in 20th century coupled simulations, *Ocean Modell.*, *15*, 274–298, doi:10.1016/j.ocemod.2006.02.004.
- Guilyardi, E., A. Wittenberg, A. Fedorov, M. Collins, C. Wang, A. Capotondi, G. J. van Oldenborgh, and T. Stockdale (2009), Understanding El Niño in ocean-atmosphere general circulation models: Progress and challenges, *Bull. Am. Meteorol. Soc.*, *90*, 325–340, doi:10.1175/2008BAMS2387.1.
- Jin, F.-F. (1997), An equatorial ocean recharge paradigm for ENSO. Part I: Conceptual model, *J. Atmos. Sci.*, *54*, 811–829, doi:10.1175/1520-0469(1997)054<0811:AEORPF>2.0.CO;2.
- Kao, H.-Y., and J.-Y. Yu (2009), Contrasting eastern-Pacific and central-Pacific types of El Niño, *J. Clim.*, *22*, 615–632, doi:10.1175/2008JCLI2309.1.
- Kirtman, B. P. (1997), Oceanic Rossby wave dynamics and the ENSO period in a coupled Model, *J. Clim.*, *10*, 1690–1704, doi:10.1175/1520-0442(1997)010<1690:ORWDAT>2.0.CO;2.
- Knutson, T. R., and S. Manabe (1998), Model assessment of decadal variability and trends in the tropical Pacific Ocean, *J. Clim.*, *11*, 2273–2296, doi:10.1175/1520-0442(1998)011<2273:MAODVA>2.0.CO;2.
- Kug, J.-S., F.-F. Jin, and S.-I. An (2009), Two types of El Niño events: Cold tongue El Niño and warm pool El Niño, *J. Clim.*, *22*, 1499–1515, doi:10.1175/2008JCLI2624.1.
- Larkin, N. K., and D. E. Harrison (2005), On the definition of El Niño and associated seasonal average U.S. weather anomalies, *Geophys. Res. Lett.*, *32*, L13705, doi:10.1029/2005GL022738.
- Meehl, G. A., H. Teng, and G. W. Branstator (2006), Future changes of El Niño in two global coupled climate models, *Clim. Dyn.*, *26*, 549–566, doi:10.1007/s00382-005-0098-0.
- Neale, R. B., J. H. Richter, and M. Jochum (2008), The impact of convection on ENSO: From a delayed oscillator to a series of events, *J. Clim.*, *21*, 5904–5924, doi:10.1175/2008JCLI2444.1.
- Rasmusson, E. M., and T. H. Carpenter (1982), Variations in tropical sea surface temperature and surface wind fields associated with the Southern Oscillation/El Niño, *Mon. Weather Rev.*, *110*, 354–384, doi:10.1175/1520-0493(1982)110<0354:VITSST>2.0.CO;2.
- Rayner, N. A., D. E. Parker, E. B. Horton, C. K. Folland, L. V. Alexander, D. P. Rowell, E. C. Kent, and A. Kaplan (2003), Global analyses of sea surface temperature, sea ice, and night marine air temperature since the late nineteenth century, *J. Geophys. Res.*, *108*(D14), 4407, doi:10.1029/2002JD002670.
- Smith, T. M., and R. W. Reynolds (2003), Extended reconstruction of global sea surface temperatures based on COADS data (1854–1997), *J. Clim.*, *16*, 1495–1510.
- Timmermann, A. (1999), Detecting the nonstationary response of ENSO to greenhouse warming, *J. Atmos. Sci.*, *56*, 2313–2325, doi:10.1175/1520-0469(1999)056<2313:DTNROE>2.0.CO;2.
- Yu, J.-Y., and H.-Y. Kao (2007), Decadal changes of ENSO persistence barrier in SST and ocean heat content indices: 1958–2001, *J. Geophys. Res.*, *112*, D13106, doi:10.1029/2006JD007654.

S. T. Kim, and J.-Y. Yu, Department of Earth System Science, University of California, 3315 Croul Hall, Irvine, CA 92697-3100, USA. (jyyu@uci.edu)